Additive Manufacturing 89 (2024) 104304

Contents lists available at ScienceDirect

Additive Manufacturing

journal homepage: www.elsevier.com/locate/addma

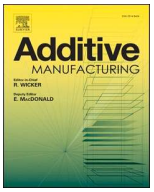

High-resolution 3D printable inks based on functional polymeric ionic liquids for applications in carbon dioxide valorization

Simone Marchetti [a,b], Cristopher Tinajero [a], Gianluca Palmara [a], Eduardo García-Verdugo [c], Ignazio Roppolo [b], Marcileia Zanatta [a,d,*], Victor Sans [a,**]

[a] Institute of Advanced Materials (INAM), Universitat Jaume I, Avda Sos Baynat s/n, Castellón 12071, Spain
[b] Dipartimento di Scienza Applicata e Tecnologia, Politecnico di Torino, C.so Duca degli Abruzzi 24, Turin 10129, Italy
[c] Departamento de Química Inorgánica y Orgánica, Grupo de Química Sostenible y Supramolecular Universidad Jaume I, Castellón E-12071, Spain
[d] Departament de Química Física i Analítica, Universitat Jaume I, Avda Sos Baynat s/n, Castellón de la Plana 12071, Spain

ARTICLE INFO

Keywords:
3D printing
High-resolution
Polymeric ionic liquids
CO_2 conversion
Cyclic carbonate
Continuous flow

ABSTRACT

This study investigates the use of epoxy-functionalized acrylate-based 3D printable ink for creating high-resolution functionalized devices, exploring the possibility to further functionalize those for chemical engineering applications. In fact, the control of the epoxy-functionalized surface enables the formation of active surfaces, and this study employs supported Ionic Liquids with catalytic properties as a proof of concept. Ionic liquids (ILs) and polymeric derivatives represent a promising path to generate multifunctional complex 3D structures, playing advanced roles in multiple applications. The fine-tuning of the functionalization methodology and formulation enhances the resolution of acrylate-based resins, allowing the production of highly detailed structures that can significantly boost catalytic efficiency. Through a comparison with commercial resins, the developed formulation demonstrates superior resolution capabilities, positioning it as an effective alternative for use in vat photopolymerization technologies. Additionally, controlling the level of functionalization and accessibility of the ILs' active sites through the control of the surface area of the reactor has led to improved process performance in terms of yield and space-time yield (STY) in the CO_2 cycloaddition to epoxide reaction.

1. Introduction

Additive manufacturing, also known as 3D printing, is rapidly impacting a large number of scientific and technological areas. The possibility of rapidly generating digital structures, novel geometries not possible with traditional manufacturing and the ability to rapidly fabricating them, opens a wealth of possibilities for new devices and applications in numerous fields, including aerospace, automotive, food, bioprinting, catalysis, optoelectronics [1–3]. Across the miriad of applications and technologies being developed, there is a common thread in the need to develop inks and precursor materials capable to deliver high-resolution printing capabilities. Crafting formulations that simultaneously meet the necessary processing properties and functionality for cutting-edge applications presents a significant challenge [4]. Among the different 3D printing techonologies, the one based on vat photopolymerization appears particularly suitable for developing complete structures with functional properties [5–7]. Within this technological landscape, ionic liquids (ILs) and polymeric derivatives have emerged as a promising avenue for creating 3D multifunctional structures, with a broad range of applications, as energy storage, photocatalysis, biomedical, CO_2 transformation [8–10]. In this context, vat photopolymerization is gaining importance also in carbon dioxide capture and valorization [11].

The escalating levels of carbon dioxide (CO_2) in the atmosphere is dictating an urgent environmental challenge. Addressing this issue requires innovative approaches to capture and transform CO_2 into valuable compounds [12]. The synthesis of cyclic carbonates from epoxides and CO_2 involves a gas–liquid process where mass transfer from the gas phase to the liquid phase precedes a catalytic cycloaddition reaction. In traditional batch reactors, the rate of CO_2 mass transfer has been identified as a crucial factor controlling the reaction rate [13]. However, these batch reactors face efficiency, cost, and safety challenges. Continuous flow systems offer a promising alternative with advantages such as lower reaction temperatures, shorter residence times, and

* Corresponding author at: Institute of Advanced Materials (INAM), Universitat Jaume I, Avda Sos Baynat s/n, Castellón 12071, Spain.
** Corresponding author.
E-mail addresses: zanatta@uji.es (M. Zanatta), sans@uji.es (V. Sans).

https://doi.org/10.1016/j.addma.2024.104304
Received 15 March 2024; Received in revised form 19 June 2024; Accepted 6 July 2024
Available online 10 July 2024

scalability for industrial applications [14]. Recent developments in flow chemistry have opened new opportunities for the transformation of CO_2 into valuable organic compounds. Continuous flow reactors, with their large surface-to-volume ratio, enable effective mixing of phases and precise temperature control, enhancing heat and mass transfer and improving reaction efficiency [15]. Additionally, the safety and efficiency of flow reactors make them suitable for challenging transformations that are hard to achieve in batch reactors [16,17].

More specifically, advances in the synthesis of cyclic carbonates within flow reactors showcase diverse strategies and catalysts employed to address the challenges of carbon dioxide (CO_2) utilization [18–27]. Zhang et al. (2015) used a packed-bed reactor with coconut shell activated carbon (CSAC) anchored ionic liquids, achieving an 82 % yield in the cycloaddition of epichlorohydrin at 1.4 MPa and 140 °C [22]. Valverde et al. (2019) used multifunctional polymers based on ionic liquids and Rose Bengal fragments in a continuous flow reactor, achieving a 53 % conversion over 10 days [28]. Microreactors were also employed to reduce residence time, with Li et al. (2018) demonstrating 90–99 % conversion in less than 100 seconds using a binary catalytic system [29]. Yin et al. (2021) utilized a packed bed reactor with a green DBU-based IL catalyst (DBU@SBA), achieving a 57 % conversion after 2 hours [23]. The use of PIL based aerogels in packed-bed reactors have shown a STY of 21.18 $g_{prod}\ h^{-1}\ L^{-1}$ [30]. While flow chemistry presents numerous advantages for CO_2 transformation, challenges persist. The low reactivity of CO_2, coupled with the challenges associated with the employment of heterogeneous catalysts, including maldistribution of flow patterns influenced by reactor geometry and operating conditions, necessitates adjustments in operating parameters for continuous processes. The development of innovative approaches, like the use of 3D printing (3DP) techniques stands out for the devlopment of advanced reactor architectures [31].

Recently we demonstrated that 3D printed catalytic reactors perform better under continuous-flow than traditional packed bed reactors for the cycloaddition reaction at laboratory scale [28,32]. Nevertheless, the fully exploitation of this novel concept requires to maximize the active surface area and the possibility to fabricate structures with high-resolution. This paper presents a new formulation that offers the possibility to achieve high resolution 3DP reactors. Additionally, it optimizes the functionalization protocol to effectively incorporate the required IL-based moieties that act as catalysts. By fine-tuning all these parameters, a high-resolution 3DP reactor achieves a good level of activity and productivity towards the synthesis of cyclic carbonates through the selective cycloaddition of CO_2 to epoxides.

2. Results and discussion

This study explores two unique monomeric formulations, labeled F1 and F2, which are based on Glycidyl Methacrylate (GMA). In our prior work, we reported functional 3DP inks using GMA; however, the resolution of these inks was insufficient for fabricating highly complex geometries, achieving a maximum resolution of *ca.* 500 μm. Here, different cross-linkers were used, aiming at precisely tailoring the resolution of the 3DP structures. In particular, here two distinct acrylate-based were tested: the first one based on the bifunctional 1,4-Butanediol Diacrylate

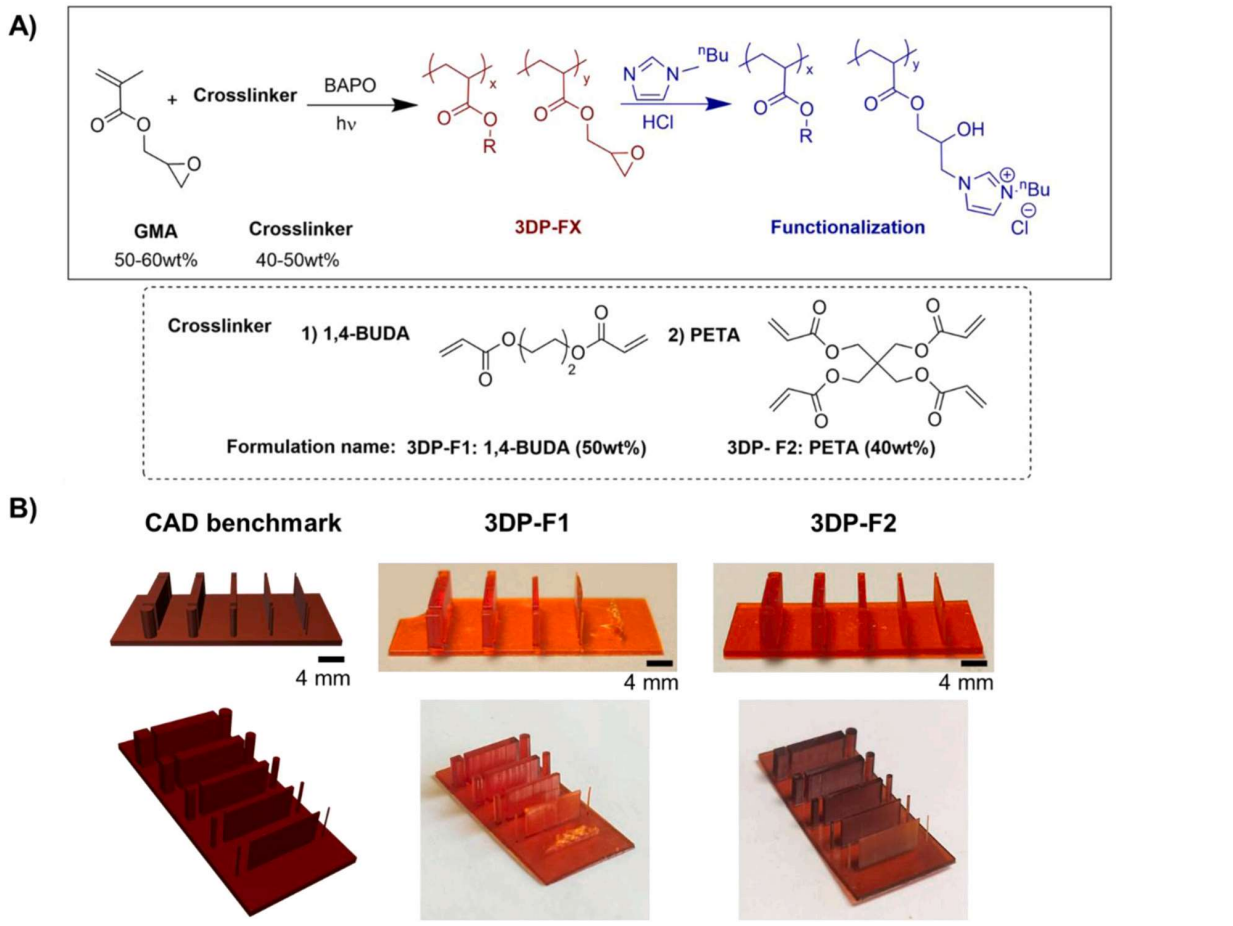

Fig. 1. A) Formulation used in this work. B) Benchmark CAD design with 5 different thicknesses (*2.0*, *1.5*, *1.0*, *0.5,* and *0.25 mm*) and 3DP figures using different polymeric formulations.

(BUDA) (**3DP-F1**), while the second one was based on Pentaerythritol Tetraacrylate (PETA) (**3DP-F2**), a tetrafunctional monomer. In both monomeric mixtures Phenylbis(2,4,6-trimethylbenzoyl)phosphine oxide (BAPO) was added as a photoinitiator (Fig. 1**A**). A summary of all the formulations involved in the optimization process is reported in Table S1 of the Supporting Information.

A preliminary exploration of the 3DP-F1 formulation has been previously conducted and published [33]. During this initial study, resolution was identified as a critical parameter requiring further optimization. In a first attempt, the amount of photoinitiator employed (BAPO) was optimized in the range (0.5 % - 2 %) for the formulation (**3DP-F1**) composed of a mixture (1:1w/w) of GMA and BUDA. Despite all the efforts to optimize the printing parameters, the resolution achieved for spiral-shaped (Figure S1) and benchmark (Fig. 1**B**) structures remained unsatisfactory (Figure S2). An increase in the amount of BUDA crosslinker was attempted, but this did not enhance the resolution and resulted in a reduction of functional epoxide groups on the polymer surface. As the research progressed, the need for higher resolution and an increased percentage of GMA to improve catalyst distribution on the surface was recognized. Consequently, an alternative approach was pursued, employing a different cross-linker rather than increasing the existing one, building upon a previously optimized formulation to achieve these improvements. This encouraged the exploration of a new formulation (**3DP-F2**), characterized by the use of PETA, well-known crosslinker for giving resins with high resolution [30,34], primarily due to two key factors: (1) as a tetrafunctional monomer, PETA requires very low exposure times to form a cross-linked network and reach the gel point; these low exposure times result in lower light doses, thereby allowing more controlled penetration of light [35]. (2) The highly cross-linked network formed by PETA restricts the mobility of growing macroradicals, thereby limiting the propagation of the polymerization reaction beyond the initial irradiated area. This crosslinker allowed also to increase the weight percentage of GMA (from 50 wt% in F1 to 60 wt% in F2; see experimental section for more details). These modifications also allowed to an increase in the concentration of epoxy groups, including on the surface, which is a key factor for an efficient post-functionalization step with IL moieties. Additionally, other adjustments were necessary to obtain structures with high resolution, which include the control of exposure parameters in vat photopolymerization printer Mars 3 Pro, but also the introduction of other additives, such as a dye, *Methyl Red*, and a radical scavenger, *Pentaerythritol tetrakis (3,5-di-tert-butyl-4-hydroxyhydrocinnamate)*, which role in enhancing print fidelity and resolution (Figure S3) is well known [35]. The optimized parameters were obtained from Jacobs' working curve (Figure S4 and Table S2) [36], which allowed to estimate the exposure time required for the polymerization of a 50 μm layer for the two formulations; 3DP-F2 required a lower exposure energy in order to generate a cross-linked network when compared to 3DP-F1 formulation, supporting the initial idea that using PETA as a crosslinker could improve the printability of the formulation with respect to the one employing BUDA, as showcased in the pictures of the benchmark structure (Fig. 1B). Noteworthy, with 3DP-F2 formulation it was possible to print the smallest feature tested (250 μm), which was not achievable with 3DP-F1.

For the sake of completeness, images of specimens produced with non-optimized parameters and obtained under various conditions are included in the Supporting Information (Figures S1-S3) to illustrate the importance of an optimized printing process. These examples demonstrate that incomplete or uncontrolled polymerization occurs when printing parameters are not optimized. Consequently, the best conditions identified are reported in the methods section and used for the following experiments.

At last, for comparison purposes, a commercial resin (Standard Translucent Photopolymer Resin by Elegoo, **3DP-COMM**) was also tested for printing the benchmark employing the optimized manufacturer's settings (see experimental data for more details). Noteworthy, the formulation **3DP-F2** exhibited equivalent resolution to the commercial resin for this design (see Figures S5-S6 and Table S3 for a quantitative comparison**)**.

2.1. Reactor design

In the pursuit of optimizing the performance of 3DP reactor structures, the design of the printed objects plays a crucial role. After the identification of the best formulation explored (**3DP-F2**), different designs were generated and tested to assess the structural integrity and the fit for the envisioned application as a catalytic structured reactor.

Based on our previous studies, which showcased the efficacy of spiral structures in converting CO_2 into cyclic carbonates [32], adjustments were made to the helix pitch, and slender columns were incorporated into the structure to bolster strength and improve flow conditions. For example, Fig. 2**A** illustrates the design generated through the reactor's structural optimization process, whereby four different helix pitches were used ranging from 4 to 1.2 mm. The high resolution demonstrated by the **3DP-F2** formulation enabled the printing of larger devices with well-resolved features (Fig. 2**B**).

A significant accomplishment was the successful printing of an 11 cm spiral with a minimal pitch of 1.2 mm. This corresponds to an approximate 0.6 mm gap between solid layers, qualifying it as a microreactor in reactor engineering contexts. Based on our experience, a helix pitch of 1.2 mm is the finest feature that can be reliably produced with current technology. The pitch represents a full 360º rotation of the helix, with the gap between solid surfaces around 0.6 mm and the helix thickness under 0.2 mm. This setup approaches the maximum resolution that our current technology and formulation can achieve. Attempting to reduce the pitch further might compromise the structural integrity and consistency of the printed reactors, as the current technology does not support the reliable creation of finer features. Thus, while theoretically, a smaller pitch could increase surface area and potentially enhance reactor efficiency, practical limitations require maintaining the pitch at 1.2 mm to ensure the reproducibility and structural stability of the fabricated microreactor designs.

The high level of fidelity of the printing process was demonstrated by 3D scanning the printed part and comparing it to the original CAD (Fig. 2**C**). Remarkably, when a part with a 4 mm helix pitch was printed with the resin **3DP-F2**, the resolution observed by optical microscopy (Fig. 2**D)** showed a very good level of detail and high fidelity. Challenges with the commercial resin, attributed to viscosity and short printing times, hindered the efficient flow of resin away from the structure before subsequent layers were cured. Further optimization of the printing parameters could have led to comparable performance of the commercial resin. However, this comprehensive indicative structure presents advancements in terms of the printability of complex structures with **3DP-F2**. Hence, it enables the fabrication of large parts with high resolution and complex features. As a proof of concept, the spiral-based structures were packed in glass columns and applied as structured continuous-flow catalytic chemical reactors. A previously determined swelling of 1–5 % was taken into account when printing the structured helicoidal reactors to fit exactly in the column [32].

2.2. Optimization of polymeric surface functionalization

To improve the functionalization process previously reported by us [33], we evaluated different strategies based on the nucleophilic ring opening of epoxides. The functionalization of the 3DP structures was done in test tubes placed in an ice bath.

A systematic variation of conditions was implemented through different protocols (Fig. 3). This included variation of solvent, UV light post-curing (15 min, 60 ºC, 405 nm) (before or after the functionalization reaction), and the reagent addition order, either simultaneously (one pot), or sequentially (2 steps: *(i)* HCl; *(ii)* butylimidazol). The reagents employed were HCl to open the epoxide of the GMA to form a

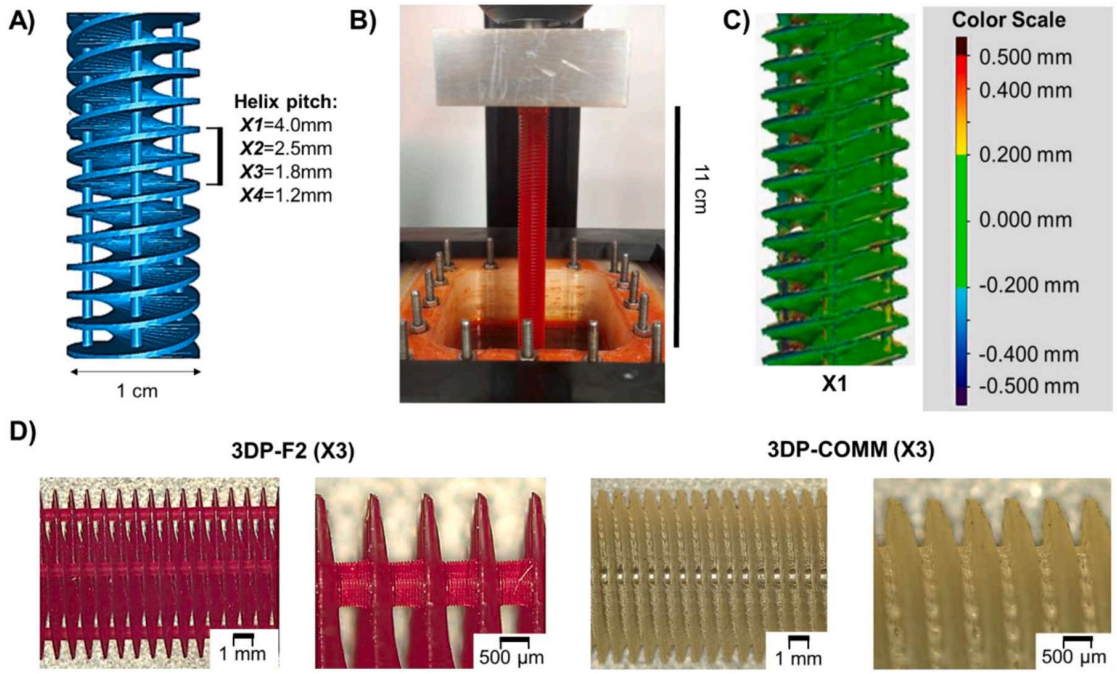

Fig. 2. Helicoidal design and fabrication under optimized conditions. A) CAD file of 3DP functional devices. B) Photo of 3DP structure using VAT polymerization. C) 3D Scanned image of part 3DP-F2 (X1). (D) Microscopic images obtained for the formulations 3DP-F2 (X3) and the 3DP-COMM (X3).

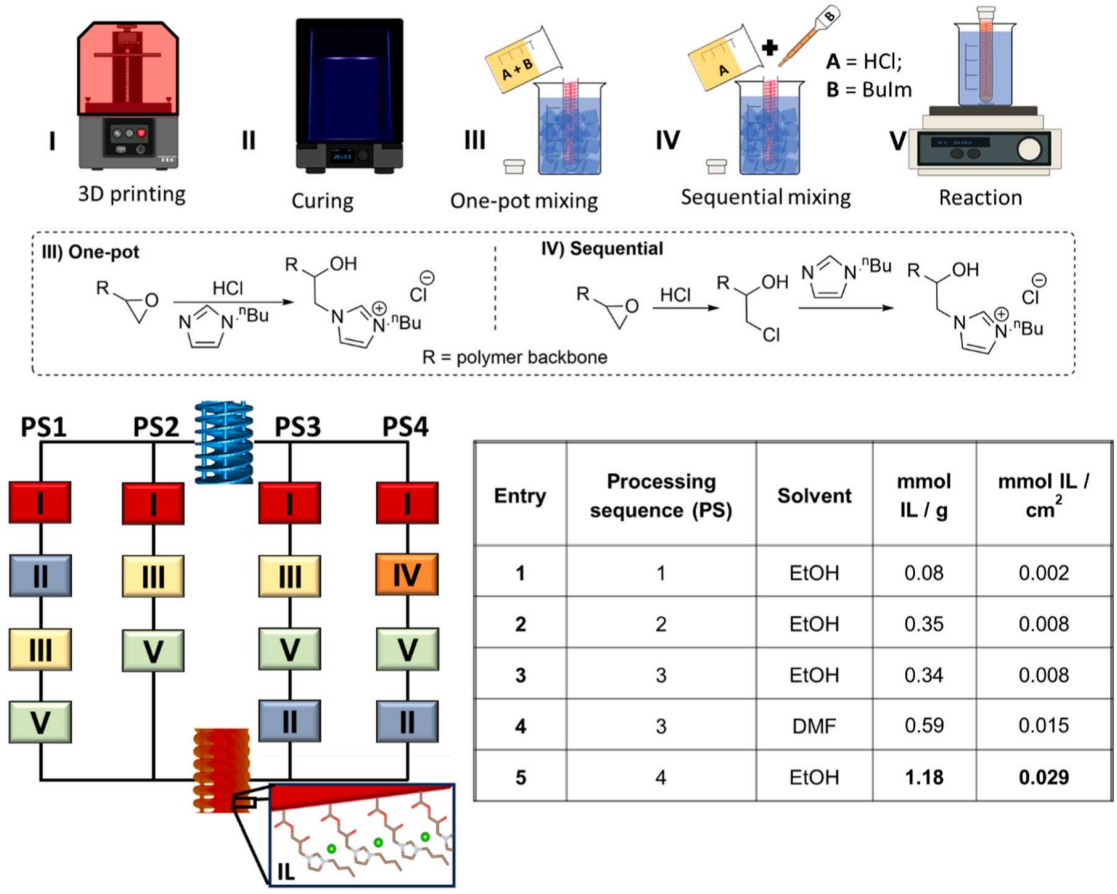

Entry	Processing sequence (PS)	Solvent	mmol IL / g	mmol IL / cm^2
1	1	EtOH	0.08	0.002
2	2	EtOH	0.35	0.008
3	3	EtOH	0.34	0.008
4	3	DMF	0.59	0.015
5	4	EtOH	**1.18**	**0.029**

Fig. 3. Functionalization methodologies and IL loading (calculated from elemental analysis) according to the processing sequence (PS) followed.

surface bound halohydrin and butyl imidazole to form the IL species in the surface. The quantities of hydrochloric acid and butyl imidazole were maintained at constant levels across all conditions, ensuring that observed differences could be attributed specifically to the manipulated parameters with a quantitative assessment performed through elemental analysis. The degree of functionalization of the epoxy groups is expressed in two ways: millimoles of butyl imidazole per gram of the polymer ($mmol_{IL}/g_{polymer}$) and millimoles of butyl imidazole per square centimeter of the polymer's surface area ($mmol_{IL}/cm^2_{polymer}$). These values are calculated based on the amount of nitrogen detected through elemental analysis of the modified polymer (Fig. 3**, table)**. Lower levels of functionalization were achieved when the reagent addition occurred in one step (Fig. 3**, III**), compared to a sequential addition protocol (Fig. 3**, IV**) with the subsequent dropwise addition of butyl imidazole. This nuanced approach showcased improved efficiency in introducing functional groups to the printed objects.

Moreover, the timing of UV light post-curing (**II**) exhibited a substantial influence on the functionalization process. Minimal differences were noted when post-curing was skipped (**PS2**) or performed after functionalization (**PS3**). In contrast, if post-curing was executed after printing (**PS3**) but before functionalization (**PS1**), there was a notable reduction of approximately four times in the IL mmol count (from 0.34 to 0.08 $mmol_{IL}/g_{polymer}$). This can be attributed to a higher level of superficial cross-linking due to the conversion of residual double-bonds created by the UV post-curing process. This could reduce the accessibility of the reagents to active epoxide sites in the resin not directly located in the surface of the polymers. This underscores a critical consideration: the preference for either omitting post-curing or conducting it after functionalization to maximize the introduction of functional groups. A two-step functionalization in EtOH, where in first place the HCl performs a ring opening to form the corresponding halohydrins, with subsequent dropwise addition of butyl imidazole, led to a

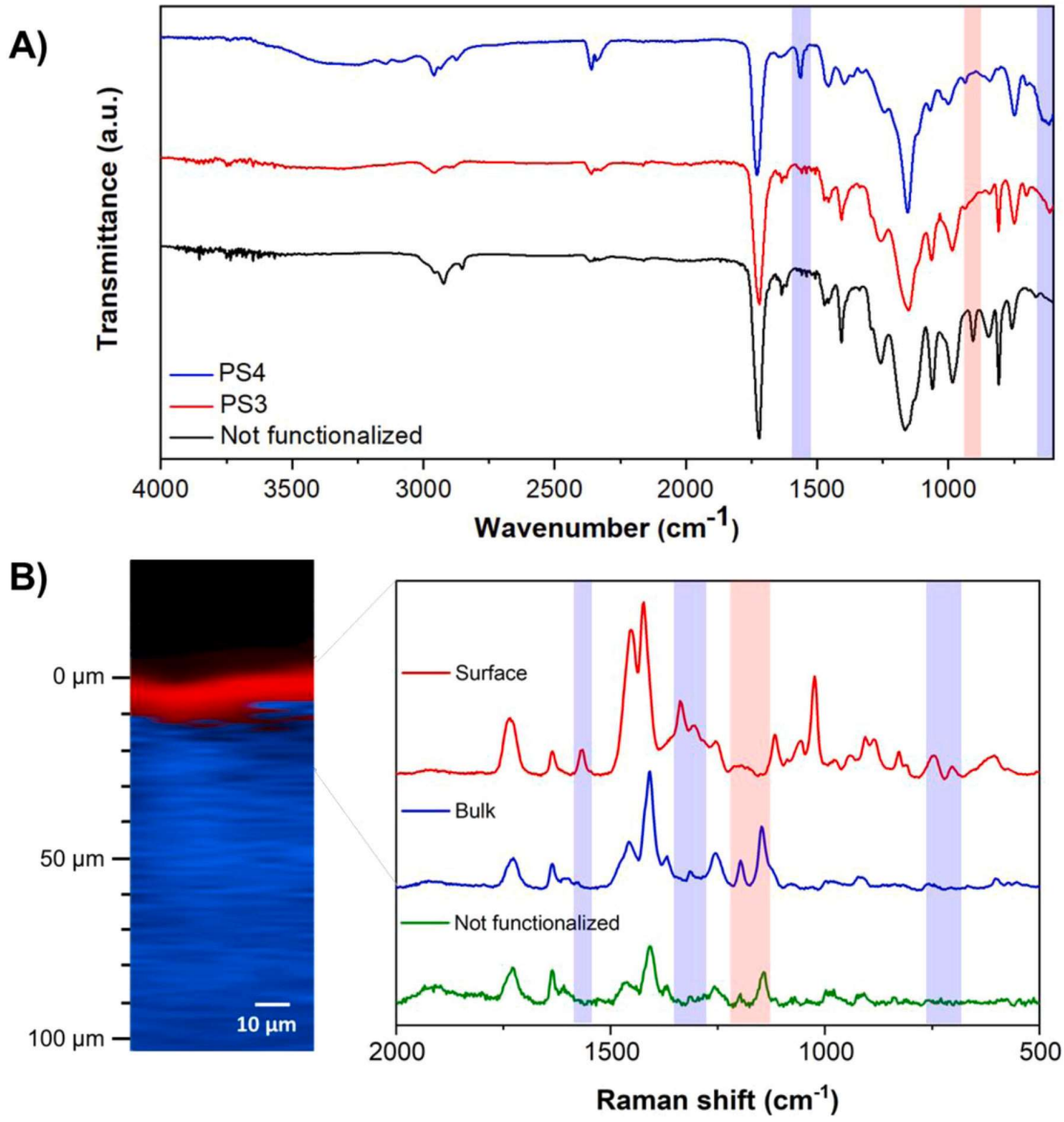

Fig. 4. Characterization of **3DP-F2** formulation. A) FTIR-ATR spectra of the polymeric material before modification (in black) and after imidazolium functionalization with **PS3** (red) and **PS4** (blue) protocols. B) (Left) Mapping for the initial 100 µm depth of a 3D printed **PS4** resin: the red region corresponds to the surface modification with imidazolium units, and the blue region corresponds to the unmodified epoxy region. (Right) Raman spectra corresponding to the blue (surface) and red (core polymer) regions.

significantly higher degree of functionalization (**PS4**), when compared to a one-pot functionalization with both the HCl and the butyl imidazole added simultaneously (**PS3**) (1.18 vs. 0.34). This is likely because HCl, being a strong acid, protonates the oxygen of the epoxide, significantly increasing the electrophilicity of the epoxide carbon. This step is crucial as it makes the carbon more susceptible to nucleophilic attack (of Cl- in this case), facilitating the ring opening of more epoxide centers. In addition, the formation of a halohydrin probably changes the hydrophobicity of the resin, making it a more suitable precursor for the formation of the surface-bound IL than when both substrates are added simultaneously (**PS4**), where an imidazolium salt is formed and act as nucleophile, thus hindering its surface reactivity. The functionalization of the synthetic sequences **PS3** and **PS4** were characterized by FTIR spectra (Fig. 4A), following the disappearance of epoxy groups at 905 cm^{-1} (C-O stretching, highlighted in red) of the GMA and the appearance of specific bands related to the imidazole ring in butyl imidazole at 1560 cm^{-1} (C═N ring stretching) and around 625 cm^{-1} (out-of-plane ring vibrations), highlighted in blue. Comparisons between different conditions indicated that the PS4 (red spectrum) resulted in a higher degree of functionalization, as evidenced by the appearance of expected changes in the spectra. When PS3 protocol was employed (blue spectrum), the anticipated imidazolium stretching bands were much weaker, thus corroborating a lower degree of functionalization.

The spatial distribution of the IL moieties was probed with Raman confocal microscopy analysis of the materials produced with PS4. This technique enabled the mapping of polymer composition with a penetration depth of about 100 μm. Fig. 4B (left) shows the mapping obtained for the functionalized material, utilizing different penetration depths for the incident laser light. The figure reveals two distinct regions: (i) the red region (from 0 to 10 μm) indicating surface modification with imidazolium units, and (ii) the blue region (from 10 to 100 μm) representing the bulk of the material (not functionalized). Furthermore, the Raman spectra (Fig. 4B, right) of each of these two regions illustrate the main differences between the pristine materials and the functionalized material. Analysis of the Raman spectrum of the bulky polymer (blue spectrum) and the non-functionalized sample (green spectrum), indicates the presence of epoxy groups, with peaks at 1145 cm^{-1} and 1195 cm^{-1} (highlighted in red). This peak disappears in the spectra of the surface (red spectrum), indicating epoxide ring opening. Additionally, in the Raman spectra of the surface, it is possible to observe the emergence of new peaks (highlighted in blue), at 1335 cm^{-1}, 1565 cm^{-1}, and between 767 cm^{-1} and 685 cm^{-1}, attributable to imidazolium substitution, confirming the success of the surface functionalization.

Finally, DSC and TGA analyses of the material before and after functionalization were conducted (Figure S7). However, no significant changes in degradation behavior or crystallization were observed in these analyses.

These findings not only contribute to the nuanced understanding of the functionalization process but also provide practical insights for maximizing the functional potential of 3D-printed objects using the **3DP-F2** formulation.

2.3. CO_2 valorization

A continuous-flow automated rig (Vapourtec R400) was employed for the evaluation of the catalytic performance of the different

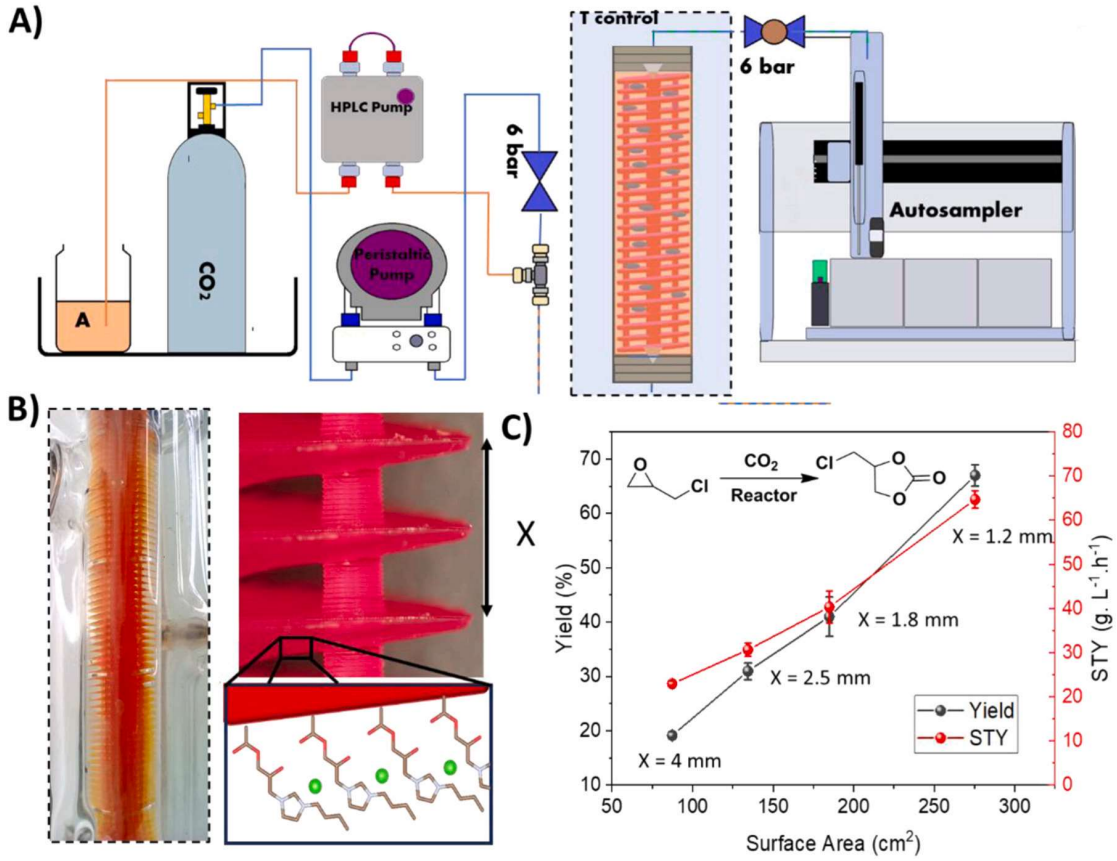

Fig. 5. CO_2 valorization experiments performed with catalytic 3DP structured reactors. A) Schematic representation of the rig employed. B) Optical images of the packed helicoidal 3DP catalytic reactor. C) Results corresponding to the cycloaddition reaction between ECH and CO_2, determined by NMR analysis (Fig. S8). *Reaction conditions:* ECH solution (2 M in IPA) (flow rate = 50 μL.min^{-1}), CO_2 (flow rate = 41 μL.min^{-1}), 120 °C, 6 bar, with a residence times 50–63 min.

geometries fabricated (Fig. 5**A**). The optimized protocol to maximize the amount of IL loading was applied to the **3DP-F2** geometries and the resulting devices were packed in glass columns (Fig. 5**B**) and integrated in the reaction platform. The reaction between epichlorohydrin (ECH) and CO_2 was performed under biphasic conditions, employing an HPLC pump to pump the liquid phase and a peristaltic pump (Vapourtec R2) for the gas (Fig. 5**A**). The reaction was performed under continuous-flow steady-state conditions of pressure (6 bar) and a temperature of 120 °C was employed. The reagents flow continuously through the structured reactor in a heterogeneous gas-liquid configuration. The catalytic activity was inversely dependent on the helicoidal pitch from the reactors. A quasi-linear correlation was observed between the yield and the space time yield (STY) and the surface area of the printed reactor (Fig. 5**C**). This is logical since the catalyst is immobilized on the surface of the reactor. Hence, higher resolution in the printing process is critical to enable more efficient performance of the structured reactors. Under the optimized conditions, a remarkable STY of 65 g L^{-1} h^{-1} was achieved, which represents an order of magnitude improvement over previously reported values in 3D printed PIL-based catalytic flow reactors [33] and four time more than packed-bed reactor (21 g h^{-1} L^{-1}) [30]. Even though these values are still below those obtained in highly intensified homogeneous systems reactor (2.7 kg h^{-1} L^{-1}) [18], the efficient immobilization of the catalysts eliminates the need for subsequent separation, thus reducing operational costs. For the 3D printed PIL-based catalytic reactor presented here, the performance could be further enhanced by increasing the number of catalytic active sites available for reaction, for example adding texture or porosity to the material. The catalytic systems demonstrated stability by maintaining consistent flow conditions for 6 hours without any decline in activity. Furthermore, a long-duration experiment exceeding 72 hours was conducted without any observed change in performance, confirming the robustness of the system. Furthermore, catalytic activity was consistent when different columns with the same configuration were employed.

3. Conclusions

This study highlights the significant potential of optimizing acrylate-based 3D printable inks for enhanced resolution and performance in catalytic applications. By fine-tuning the functionalization methodology and formulation, we have demonstrated the ability to generate highly detailed structure devices with superior resolution capabilities compared to commercial resins. The preference for omitting post-curing or conducting it after functionalization, coupled with the two-step functionalization approach in ethanol followed by dropwise addition of butyl imidazole, has proven to be superior in maximizing catalyst (IL) amount. These findings not only deepen the understanding of the functionalization process but also provide practical insights for maximizing the functional potential of 3D-printed objects. Importantly, higher resolution printing enabled more efficient performance of structured reactors, as evidenced by the remarkable space time yield (STY) achieved under optimized conditions, representing a significant improvement over previously reported value. This underscores the promising future of IL-based functionalization in advancing the capabilities of 3D printing technologies for catalytic applications.

4. Experimental section

4.1. Materials

All reagents and solvents used during this work were commercially available: 1,4-Butanediol diacrylate (90 %, Aldrich), **BUDA**; Pentaerythritol Tetraacrylate (>99 %, Aldrich), **PETA**, Glycidyl methacrylate (97 %, Aldrich), **GMA**; Phenylbis(2,4,6-trimethylbenzoyl) phosphine oxide (97 %, Aldrich), **BAPO**; Methyl Red (ACS reagent, crystalline, Aldrich), **MR**; Pentaerythritol tetrakis (3,5-di-tert-butyl-4-hydroxyhydrocinnamate) (98 %, Aldrich), Radical Scavenger; ink (ELEGOO translucent LCD UV-Curing); 1-butylimidazole (98 %, Aldrich); hydrochloric acid (37 %, Scharlab); Epichlorohydrin (98 %, Aldrich); Ethanol absolute (for analysis, Supelco); 2-Propanol (for analysis, Supelco); Dimethylformamide (VWR Chemicals).

4.2. Formulation

The formulation and 3D printing procedure were conducted based on our previous methodology with some modifications [33].

4.2.1. 3DP-F1 composition

The printer reservoir was loaded with a 50.0 mL solution consisting in 50 % by weight of GMA, 50 % by weight of BUDA, and 2 wt% of the photoinitiator (Phenyl-bis-(2,4,6-trimethylbenzoyl)phosphine oxide) regarding the monomers, 0,1 wt% Pentaerythritol tetrakis (3,5-di-tert-butyl-4-hydroxyhydrocinnamate) and 0,1 wt% Methyl Red. The 3D structure was obtained according to the digital design downloaded in the printer (short fusilli with different helix pitches).

4.2.2. 3DP-F2 composition

The printer reservoir was loaded with a 50.0 mL solution consisting in 60 % by weight of GMA, 40 % by weight of PETA (corresponding to 1 Eq. PETA: 3,7 Eq. GMA), and 2 wt% of the photoinitiator (Phenyl-bis-(2,4,6-trimethylbenzoyl)phosphine oxide) regarding the monomers, 0,1 wt% Pentaerythritol tetrakis (3,5-di-tert-butyl-4-hydroxyhydrocinnamate) and 0,1 wt% Methyl Red. The 3D structure was obtained according to the digital design downloaded in the printer (devices X1, X2, X3 and X4).

4.2.3. Commercial resin (3DP-COMM)

The printer reservoir was loaded with a 50.0 mL of Standard Translucent Photopolymer Resin. The 3D structure was obtained according to the digital design downloaded in the printer (devices X1, X2 and X3).

4.3. 3D printing methodology

First, a 3D model was created using Solidworks as the CAD software. This model was then converted into the STL file format. Next, the STL file was imported into specialized slicing software installed on the printer. The software allowed for adjustment of printing parameters such as layer thickness, exposure time, and light intensity. Additionally, the software enabled the creation of necessary supports for overhanging or intricate features to ensure successful printing.

After the printing was completed, post-processing steps were carried out to finalize the printed object, such as removing the object from the build platform or the resin vat, washing it thoroughly with IPA (3 ×25 mL) to remove any uncured resin and post-curing at 60 °C for 15 min under UV lamp.

4.3.1. 3DP parameters for 3DP-F1

Layer Thickness: 0.05 mm; Burn-in/Bottom layers: 10; Burn-in/Bottom exposure time: 42 s/layer. Normal exposure time: 37 s/layer; Waiting time (after exposure): 2.5 s.

4.3.2. 3DP parameters for 3DP-F2

Layer Thickness: 0.05 mm; Burn-in/Bottom layers: 10; Burn-in/Bottom exposure time: 22 s/layer. Normal exposure time: 18 s/layer; Waiting time (after exposure): 2.5 s.

4.3.3. 3DP parameters for commercial resin (3DP-COMM)

Layer Thickness: 0.05 mm; Burn-in/Bottom layers: 10; Burn-in/Bottom exposure time: 40 s/layer. Normal exposure time: 3 s/layer.

4.3.4. Jacobs working curve methodology protocol

The samples required for plotting Jacobs working curves related to

both 3DP-F1 and 3DP-F2 resins were obtained employing the Elegoo Mars 3 3D printer. Test samples were printed without using the platform and by displaying a circle shaped image on the LCD screen (light intensity 3 mW/cm^2) for five different exposure times (3DP-F1 from 75 to 240 seconds and 3DP-F2 from 30 to 120 seconds). With the aim of measuring the single layer cure depth (C_d), the thickness of the samples was evaluated using a digital caliper with a maximum resolution of 0.01 mm; three different samples were printed and measured for each exposure time. For each formulation, a straight line was fitted to a semi-logarithmic plot with C_d on the y-axis and the natural logarithm of the exposure energy on the x-axis. The intersection of the working curve with the x-axis represents the critical exposure energy (E_c) in mJ · cm^{-2}, while the slope represents the penetration depth (D_p) in μm, following the Working Curve equation [36]:

$$C_d = D_p \ln\left(\frac{E}{E_c}\right)$$

4.4. Functionalization

Hydrochloric acid and solvent were initially combined in a beaker under an ice bath, followed by the gradual addition of drops of butyl imidazole, or alternatively, all components were added simultaneously. The precise molar quantities (6.5 mmol of butyl imidazole and 6.5 mmol of hydrochloric acid per 1 mL of solvent) was used to ensure complete coverage of the substrate. After removing the beaker from the ice, the object was left immersed in the solution at a temperature of 40 on a magnetic stirrer (260 rpm) for a duration of 24 hours. Once the required 24-hour period had elapsed, the object was washed with isopropanol (IPA) in three consecutive cycles of 25 mL each and subsequently dried at 60°C under vacuum overnight.

4.4.1. Cycloaddition reaction

The reaction was conducted under conditions similar to those previously described[32]. The reaction mixture was composed of a 1 M solution of epichlorohydrin in isopropyl alcohol (IPA). The reaction was carried out using a Vapourtec flow system, consisting of crucial components such as the 'R-4 Flow Reactor Heater' module, the 'R2S Pumping Module' equipped with two peristaltic pumps, and the 'R2C Pumping Module' featuring two HPLC-type pumps. Additionally, the system was linked to an autosampler to facilitate automated sample collection. All these modules and systems were remotely controlled through a UA-OPC communication protocol, utilizing Python-developed software for this purpose.

The mixture was created by a combination of a liquid phase, pumped at a rate of 0.05 mL·min^{-1} using an HPLC pump and the simultaneous pumping of gaseous CO_2 with an integrated peristaltic pump (Vapourtec R400, R2 module). A cartridge back-pressure regulator (BPR) of 6 bar was placed at the exit of the peristaltic pump to ensure a consistent gas pumping. The measured CO_2 flow rate was determined to be 41 μL·min^{-1} employing inverted burettes to calculate the displaced volume of liquid per unit of time. The reagents were combined in a T-mixer and introduced in the column at room temperature.

Under the system's pressure conditions, this calculation provided the actual CO_2 inlet flow rate. The experiment took place within a column reactor housing the 3DP structure, operating at a temperature of 120°C and a pressure of 6 bar, with a residence time ranging from 50 to 63 minutes based on the specific configuration of the reactor (R_1 = 50.88 min; R_2 = 61.65 min; R_3 = 61.98 min; R_4 = 63.19 min) and the volume of the reactor ranging from 4.63 to 7.75 mL (R_1 = 4.63 mL; R_2 = 5.61 mL; R_3 = 5.64 mL; R_4 = 5.75 mL). The yield was calculated by ^{1}H NMR spectroscopy.

The space time yield (STY) was calculated to determine the productivity by using the Eq. 1:

$$STY = \frac{product\ weight}{volume\ reactor \bullet residence\ time} = \frac{g_{prod}}{L \bullet h} \quad (1)$$

CRediT authorship contribution statement

Victor Sans: Writing – review & editing, Supervision, Project administration, Funding acquisition, Conceptualization. **Ignazio Roppolo:** Writing – review & editing, Supervision, Project administration, Funding acquisition, Conceptualization. **Marcileia Zanatta:** Writing – original draft, Supervision, Project administration, Funding acquisition, Conceptualization. **Gianluca Palmara:** Writing – review & editing, Investigation, Formal analysis, Data curation. **Eduardo García-Verdugo:** Writing – review & editing, Supervision, Funding acquisition, Conceptualization. **Simone Marchetti:** Writing – original draft, Visualization, Validation, Investigation. **Cristopher Tinajero:** Writing – original draft, Software, Methodology, Investigation.

Declaration of Competing Interest

The authors declare no conflict of interest

Data Availability

Data will be made available on request.

Acknowledgments

This work was supported by the projects (PID2020–119628RB-C33 and PID2021- 124695OB-C22), MCIN/AEI/10.13039/501100011033 and by (TED2021–130288B-I00) funded by MCIN/AEI/10.13039/501100011033 and the Unión Europea NextGenerationEU/ PRTR. Generalitat Valenciana is gratefully acknowledged for funding for infrastructure (IDIFEDER/2021/029), GenT (CIDEGENT 2018/036) and Santiago Grisolía Programme (CIGRIS/2021/075). This project has received funding from the European Union's Horizon 2020 research and innovation programme under the Marie Skłodowska-Curie grant agreement Horizon Europe No (GA no. 101064606). MZ thank the funding received from "la Caixa" Foundation (ID 100010434) under the fellowship number LCF/BQ/PR24/12050016. This work of I.R. was carried out within the Ministerial Decree no. 1062/2021 and received funding from the FSE REACT-EU - PON Ricerca e Innovazione 2014–2020. This manuscript reflects only the authors' views and opinions, neither the European Union nor the European Commission can be considered responsible for them.

Appendix A. Supporting information

Supplementary data associated with this article can be found in the online version at doi:10.1016/j.addma.2024.104304.

References

[1] I. Roppolo, M. Caprioli, C.F. Pirri, S. Magdassi, 3D Printing of Self-Healing Materials, Advanced Materials n/a(n/a) 2305537.
[2] D. Cafiso, S. Lantean, C.F. Pirri, L. Beccai, Soft Mechanosensing via 3D Printing: A review, Adv. Intell. Syst. 5 (6) (2023) 2200373.
[3] T.D. Ngo, A. Kashani, G. Imbalzano, K.T.Q. Nguyen, D. Hui, Additive manufacturing (3D printing): a review of materials, methods, applications and challenges, Compos. Part B: Eng. 143 (2018) 172–196.
[4] G. Gonzalez, I. Roppolo, C.F. Pirri, A. Chiappone, Current and emerging trends in polymeric 3D printed microfluidic devices, Addit. Manuf. 55 (2022) 102867.
[5] M. Shah, A. Ullah, K. Azher, A.U. Rehman, W. Juan, N. Aktürk, C.S. Tüfekci, M. U. Salamci, Vat photopolymerization-based 3D printing of polymer nanocomposites: current trends and applications, RSC Adv. 13 (2) (2023) 1456–1496.
[6] Z. Wang, Y. Guo, S. Cai, J. Yang, Three-dimensional printing of liquid crystal elastomers and their applications, ACS Appl. Polym. Mater. 4 (5) (2022) 3153–3168.

[7] M. Gastaldi, F. Cardano, M. Zanetti, G. Viscardi, C. Barolo, S. Bordiga, S. Magdassi, A. Fin, I. Roppolo, Functional dyes in polymeric 3D printing: applications and perspectives, ACS Mater. Lett. 3 (1) (2021) 1–17.

[8] X. Liu, Y. Shang, J. Zhang, C. Zhang, Ionic liquid-assisted 3d printing of self-polarized β-PVDF for flexible piezoelectric energy harvesting, ACS Appl. Mater. Interfaces 13 (12) (2021) 14334–14341.

[9] S. Miralles-Comins, M. Zanatta, V. Sans, Advanced formulations based on poly (ionic liquid) materials for additive manufacturing, Polymers 14 (23) (2022) 5121.

[10] K.R. Hossain, P. Jiang, X. Yao, X. Yang, D. Hu, X. Wang, Ionic liquids for 3D printing: Fabrication, properties, applications, J. Ion. Liq. 3 (2) (2023) 100066.

[11] M. Gillono, A. Chiappone, L. Mendola, M. Gomez Gomez, L. Scaltrito, C.F. Pirri, I. Roppolo, Study on the Printability through Digital Light Processing Technique of Ionic Liquids for CO2 Capture, Polymers 11 (12) (2019) 1932.

[12] M. Zanatta, Materials for Direct Air Capture and Integrated CO2 Conversion: Advancement, Challenges, and Prospects, ACS Mater. Au 3 (6) (2023) 576–583.

[13] D. Lokhat, A.K. Domah, K. Padayachee, A. Baboolal, D. Ramjugernath, Gas–liquid mass transfer in a falling film microreactor: effect of reactor orientation on liquid-side mass transfer coefficient, Chem. Eng. Sci. 155 (2016) 38–44.

[14] A.A.H. Laporte, T.M. Masson, S.D.A. Zondag, T. Noël, Multiphasic Continuous-Flow Reactors for Handling Gaseous Reagents in Organic Synthesis: Enhancing Efficiency and Safety in Chemical Processes, Angewandte Chemie International Edition n/a(n/a) e202316108.

[15] M. Usman, A. Rehman, F. Saleem, A. Abbas, V.C. Eze, A. Harvey, Synthesis of cyclic carbonates from CO2 cycloaddition to bio-based epoxides and glycerol: an overview of recent development, RSC Adv. 13 (33) (2023) 22717–22743.

[16] I. Rossetti, M. Compagnoni, Chemical reaction engineering, process design and scale-up issues at the frontier of synthesis: Flow chemistry, Chem. Eng. J. 296 (2016) 56–70.

[17] L. Capaldo, Z. Wen, T. Noël, A field guide to flow chemistry for synthetic organic chemists, Chem. Sci. 14 (16) (2023) 4230–4247.

[18] C. Muzyka, S. Renson, B. Grignard, C. Detrembleur, J.-C.M. Monbaliu, Intensified continuous flow process for the scalable production of bio-based glycerol carbonate**, Angew. Chem. Int. Ed. 38 (10) (2024) e202319060.

[19] D. Valverde, R. Porcar, P. Lozano, E. García-Verdugo, S.V. Luis, Multifunctional Polymers Based on Ionic Liquid and Rose Bengal Fragments for the Conversion of CO2 to Carbonates, ACS Sustain. Chem. Eng. 9 (5) (2021) 2309–2318.

[20] T.Q. Bui, L.J. Konwar, A. Samikannu, D. Nikjoo, J.-P. Mikkola, Mesoporous Melamine-Formaldehyde Resins as Efficient Heterogeneous Catalysts for Continuous Synthesis of Cyclic Carbonates from Epoxides and Gaseous CO2, ACS Sustain. Chem. Eng. 8 (34) (2020) 12852–12869.

[21] S. Cañellas, C. Ayats, A.H. Henseler, M.A. Pericàs, A highly active polymer-supported catalyst for asymmetric robinson annulations in continuous flow, ACS Catal. 7 (2) (2017) 1383–1391.

[22] Y. Zhang, Z. Tan, B. Liu, D. Mao, C. Xiong, Coconut shell activated carbon tethered ionic liquids for continuous cycloaddition of CO2 to epichlorohydrin in packed bed reactor, Catal. Commun. 68 (2015) 73–76.

[23] J. Sun, Z. Li, J. Yin, Continuous flow synthesis of propylene carbonate using DBU-based ionic liquid in a packed bed reactor, J. CO2 Util. 53 (2021) 101723.

[24] D. Rigo, R. Calmanti, A. Perosa, M. Selva, G. Fiorani, Diethylene Glycol/NaBr Catalyzed CO2 insertion into terminal epoxides: from batch to continuous flow, ChemCatChem 13 (8) (2021) 2005–2016.

[25] Y. Wu, Y. Ding, J. Xu, Y. Wang, K. Mumford, G.W. Stevens, W. Fei, Efficient fixation of CO2 into propylene carbonate with [BMIM]Br in a continuous-flow microreaction system, Green. Energy Environ. 6 (2) (2021) 291–297.

[26] N. Zanda, A. Sobolewska, E. Alza, A.W. Kleij, M.A. Pericàs, Organocatalytic and Halide-Free Synthesis of Glycerol Carbonate under Continuous Flow, ACS Sustain. Chem. Eng. 9 (12) (2021) 4391–4397.

[27] A. Rehman, A.M. López Fernández, M.F.M.G. Resul, A. Harvey, Kinetic investigations of styrene carbonate synthesis from styrene oxide and CO2 using a continuous flow tube-in-tube gas-liquid reactor, J. CO2 Util. 24 (2018) 341–349.

[28] D. Valverde, R. Porcar, P. Lozano, E. García-Verdugo, S.V. Luis, Multifunctional polymers based on ionic liquid and rose bengal fragments for the conversion of CO2to carbonates, ACS Sustain. Chem. Eng. 9 (5) (2021) 2309–2318.

[29] M.-R. Li, M.-C. Zhang, T.-J. Yue, X.-B. Lu, W.-M. Ren, Highly efficient conversion of CO2 to cyclic carbonates with a binary catalyst system in a microreactor: intensification of "electrophile–nucleophile" synergistic effect, RSC Adv. 8 (68) (2018) 39182–39186.

[30] R.V. Barrulas, C. Tinajero, D.P.N. Ferreira, C. Illanes-Bordomás, V. Sans, M. R. Carrott, C.A. García-González, M. Zanatta, M.C. Corvo, Poly(ionic liquid)-based aerogels for continuous-flow CO2 upcycling, J. CO2 Util. 83 (2024) 102771.

[31] C. Parra-Cabrera, C. Achille, S. Kuhn, R. Ameloot, 3D printing in chemical engineering and catalytic technology: structured catalysts, mixers and reactors, Chem. Soc. Rev. 47 (1) (2018) 209–230.

[32] D. Iglesias, C. Tinajero, S. Marchetti, I. Roppolo, M. Zanatta, V. Sans, Multi-step oxidative carboxylation of olefins with carbon dioxide by combining electrochemical and 3D-printed flow reactors, Green. Chem. 25 (23) (2023) 9934–9940.

[33] D. Valverde, R. Porcar, M. Zanatta, S. Alcalde, B. Altava, V. Sans, E. García-Verdugo, Towards highly efficient continuous-flow catalytic carbon dioxide cycloadditions with additively manufactured reactors, Green. Chem. 24 (8) (2022) 3300–3308.

[34] H. Goodarzi Hosseinabadi, D. Nieto, A. Yousefinejad, H. Fattel, L. Ionov, A.K. Miri, Ink material selection and optical design considerations in DLP 3D printing, Appl. Mater. Today 30 (2023) 101721.

[35] A. Salas, M. Zanatta, V. Sans, I. Roppolo, Chemistry in light-induced 3D printing, ChemTexts 9 (1) (2023) 4.

[36] S. Nechausov, A. Ivanchenko, O. Morozov, A. Miriyev, I. Must, O. Platnieks, M. Jurinovs, S. Gaidukovs, A. Aabloo, M. Kovač, B. Bulgakov, Effects of ionic liquids and dual curing on vat photopolymerization process and properties of 3d-printed ionogels, Addit. Manuf. 56 (2022) 102895.